nature geoscience
SUPPLEMENTARY INFORMATION
DOI: 10.1038/NGEO1295

# A deep mantle origin for the primitive signature of Ocean Island Basalt

Frédéric Deschamps[1], Edouard Kaminski[2], and Paul J. Tackley[1]

[1]Institute of Geophysics, Swiss Federal Institute of Technology Zurich, 8092 Zurich, Switzerland
[2]Institut de Physique du Globe, Sorbonne Paris Cité, Université Paris Diderot, UMR CNRS 7154, 75005 Paris, France

## Supplementary information

### Seismic signature of high pressure MORB

To test the hypothesis that MORB alone may explain the seismic velocity anomalies observed in the deep mantle, we used mineral physics data to calculate shear-wave velocity and density anomalies that would be induced by high pressure MORB.

First, we calculated sensitivities of shear-wave velocity and density to MORB and temperature using Perple_X[S1] and a recent mineral physics database[S2]. We use pyrolite as a reference composition, and we accounted for variance in the MORB composition in major oxides (CaO-FeO-MgO-$Al_2O_3$-$SiO_2$-$Na_2O$) by considering four different compositions, similar to those tested in recent models of thermo-chemical convection[S3]. Differences in MORB composition lead to differences in MORB sensitivities, which we use to estimate error bars on these sensitivities. In the layer $2670 \leq z \leq 2891$ km, we find that the sensitivities of shear-wave velocity, and density to MORB are

$$\frac{\partial lnV_S}{\partial X_{MORB}} = (1.45 \pm 0.52) \times 10^{-2}$$

and $\frac{\partial ln\rho}{\partial X_{MORB}} = (1.68 \pm 0.48) \times 10^{-2}$ ,

respectively. In the same layer, the sensitivity of shear-wave velocity and density to temperature are

DOI: 10.1038/NGEO1295

$$\frac{\partial lnV_S}{\partial T} = (-2.19 \pm 0.18) \times 10^{-5}\ \mathrm{K}^{-1}$$

and $\frac{\partial ln\rho}{\partial T} = (-1.24 \pm 0.15) \times 10^{-5}\ \mathrm{K}^{-1}$ ,

respectively. Clearly, high-pressure MORB is seismically faster and denser than the average pyrolitic mantle. Thus, to explain the large low shear-wave velocity provinces (LLVSP) observed at the bottom of the mantle, reservoirs of recycled MORB should be much hotter than average. Furthermore, shear-wave and density anomalies should be positively correlated, in contradiction with the distributions observed by normal mode tomography[S4].

Second, we used the sensitivities to MORB and temperature determined in the previous paragraph to calculate seismic anomalies induced by high pressure MORB and temperature anomalies between ± 2000 K. In the layer $2670 \leq z \leq 2891$ km, our calculations indicate that to induce a shear-wave velocity anomaly of -2.0% (typical of the anomalies observed in LLVSP), MORB should be hotter than the average mantle by about 1500 K, which is an unrealistic value (Supplementary Fig. 1). In addition, because shear-wave velocity and density anomalies have opposite sign only in a limited range of temperature, it would be difficult to explain the lack of correlation between density and shear-wave velocity anomalies.

According to these results, MORB alone may hardly explain all the observed tomographic features. An additional deep reservoir of non-pyrolitic material is thus needed to explain these observations. Probabilistic tomography suggests that the additional reservoir may be richer in iron and perovskite[S4] (excess in iron decreases shear-wave velocity but increases density, whereas excess in perovskite increases bulk-sound velocity), which is consistent with enstatite chondrite models of Earth's composition[S5]. Interestingly, recent mineral physics experiments[S6] predict an excess in iron as a result of the crystallization of a basal magma ocean. These experiments, however, also suggest a depletion in silicate.

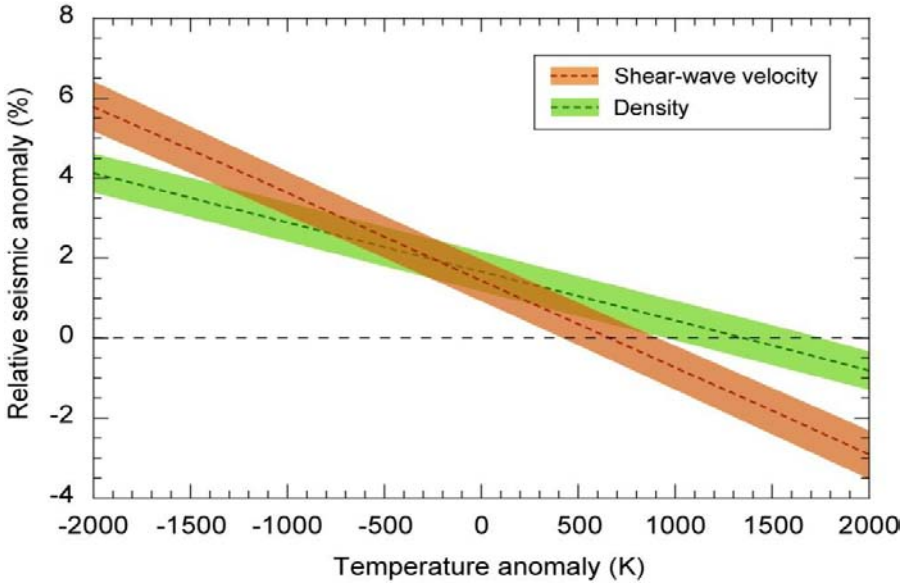


**Supplementary Figure 1 | Shear-wave velocity (red) and density (green) anomalies induced by MORB material as a function of temperature anomaly.** Anomalies are calculated in the depth range $2670 \leq z \leq 2891$ km. The thick dashed lines plot the average anomalies, and the shaded areas cover one standard deviation around these average. Sensitivities of shear-wave velocity and density were calculated using Perple_X[S1] in combination with a recent mineral physics database[S2].

## Mass balance geochemical calculations

To estimate the Helium isotopic ratio in plumes ($[^4He/^3He]_{plumes}$) as a function of the mass fraction of primitive material transported by plumes, we performed mass balance geochemical calculations[S7]. Assuming that OIB sample both the regular pyrolitic mantle and a primitive reservoir, the Helium isotopic ratio in plumes is

$$\left[\frac{^4He}{^3He}\right]_{plumes} = \alpha \left[\frac{^4He}{^3He}\right]_{PM} + (1-\alpha)\left[\frac{^4He}{^3He}\right]_{RM} \quad , \qquad (1)$$

where $[^4He/^3He]_{PM}$ and $[^4He/^3He]_{RM}$ are the Helium isotopic ratios in the primitive and regular (pyrolitic) material, respectively. A good estimate of $[^4He/^3He]_{RM}$ is given by the Helium isotopic ratio of MORB, which varies between 90000 and 120000[S8,S9,S10].

DOI: 10.1038/NGEO1295

$[^4He/^3He]_{PM}$, on the other hand, is not precisely known, and the only constraint is that it must be lower than the lowest value observed in OIB, *i.e.* 15000[S11]. The coefficient $\alpha$ is given by[S7]

$$\alpha = \frac{x_{PM} R_{He}}{1 + x_{PM}(R_{He} - 1)}, \quad (2)$$

where $x_{PM}$ is the mass fraction of primitive material entrained in the plume (or simply, entrainment). One may also use the ratio between the masses of regular and primitive materials, $r_M = M_{RM}/M_{PM} = (1 - x_{PM})/ x_{PM}$, in which case

$$\alpha = \frac{R_{He}}{R_{He} + r_M}. \quad (3)$$

In Eqs. (2) and (3), $R_{He}$ is the ratio between the concentrations in $^3He$ in the primitive and regular materials,

$$R_{He} = \frac{[^3He]_{PM}}{[^3He]_{RM}}. \quad (4)$$

The value of $[^3He]_{PM}$ depends on the initial Helium isotopic ratio, which is not well constrained. For the Earth's mantle, the value of $R_{He}$ may yield between 250 and 600[S7], corresponding to values of $[^4He/^3He]_{PM}$ between 14200 and 11500, respectively. Assuming a 1% entrainment (*i.e.*, a mass fraction of primitive material in plume equal to 1%), $[^4He/^3He]_{Plumes}$ is equal to 38500 for $R_{He}$ = 250 ($[^4He/^3He]_{PM}$ = 14200), and 24000 for $R_{He}$ = 600 ($[^4He/^3He]_{PM}$ = 11500).

The mass fraction of primitive material in plumes, $x_{PM}$, should not exceed a maximum value, $X_{PM}$, which depends on $R_{He}$ (and thus on $[^4He/^3He]_{PM}$). If $x_{PM}$ exceeds this value, the Helium isotopic ratio in plumes would be lower than the lowest value observed in OIB. To calculate $X_{PM}$ as a function of $[^4He/^3He]_{Plumes}$, one just needs to revert Eq. 1, and replace $\alpha$ by its expression (Eq. 2)

$$x_{PM} = \frac{[^4He/^3He]_{RM} - [^4He/^3He]_{Plumes}}{[^4He/^3He]_{RM} + (R_{He} - 1)[^4He/^3He]_{Plumes} - R_{He}[^4He/^3He]_{PM}}. \quad (5)$$

$R_{He}$ depends on $[^4He/^3He]_{PM}$, and here we varied its values linearly between 250 (for $[^4He/^3He]_{PM}$ = 14200), and 600 (for $[^4He/^3He]_{PM}$ = 11500). We calculated $X_{PM}$ as a function of $[^4He/^3He]_{PM}$ by fixing $[^4He/^3He]_{Plumes}$ = 15000 and $[^4He/^3He]_{RM}$ = 100000 in Eq. (5). Its value varies between about 4% and 30% for $R_{He}$ = 600 ($[^4He/^3He]_{PM}$ = 11500) and $R_{He}$ = 250 ($[^4He/^3He]_{PM}$ = 14200), respectively (Supplementary Fig. 2).

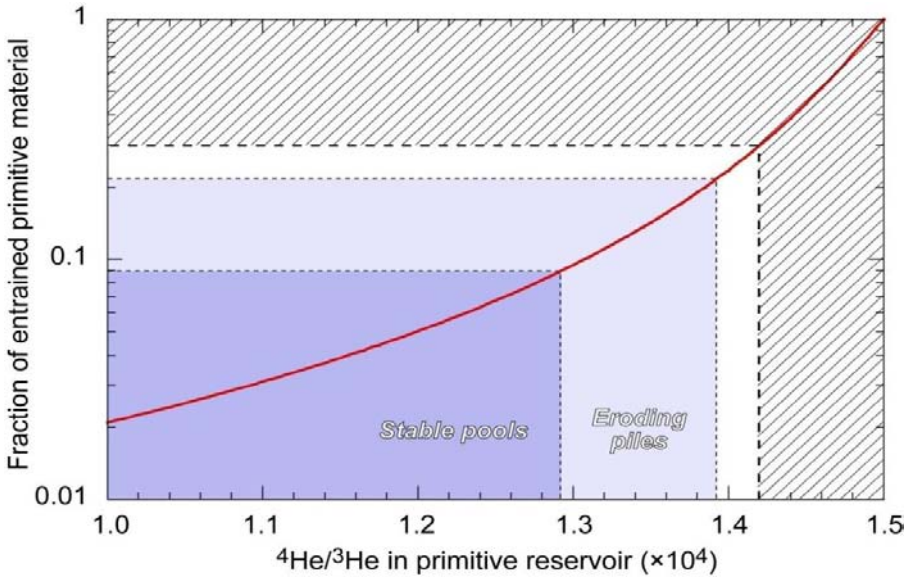


**Supplementary Figure 2 | Fraction of entrained primitive material in plumes as a function of the isotopic Helium ratio in the primitive reservoir, $[^4He/^3He]_{PM}$.** The red curve shows the fraction of primitive material in plumes that should not be exceeded ($X_{PM}$), *i.e.* the fraction of primitive material for which the isotopic Helium ratio in plumes, $[^4He/^3He]_{Plumes}$, is equal to 15000. The thick dashed line indicates the upper limit of $[^4He/^3He]_{PM}$, and the associated value of $X_{PM}$, here 30%. Larger values may be excluded. The dark blue shaded area covers the range of fraction of entrained primordial material in plumes ($x_{PM}$) predicted by models of thermo-chemical convection in which stable pools are generated, and the light blue shaded area covers all our models.

## Geodynamical modeling

The numerical experiments presented in this study were performed with StagYY[S12], which solves the conservative equations of mass, momentum, energy, and composition for an anelastic, compressible fluid with infinite Prandtl number. Calculations are made on 3D-Cartesian staggered grids (with scalar and vectorial quantities being calculated at the center

DOI: 10.1038/NGEO1295

and on the sides of each cell, respectively) of dimension 128×128×64 and aspect ratio 4. The grid spacing is vertically refined in the top and bottom parts of the system. All boundaries are free slip. The experimental setup is close to that used in previous works[S13,S14], with some modifications (see below).

The system is heated both from the bottom and from within, and the heating rate of the primitive material is increased by a factor 10. The mantle heating rate is then adjusted such that the total heat production is equivalent to a surface heat flux of 65 mW/m$^2$. Compressibility induces additional sources and sinks of heat that are controlled by the dissipation number, $Di$, which depends on the thermal expansion and thus varies with depth. In all our calculations, the surface and volume average values of the dissipation number are $Di_S = 1.2$ and $\langle Di \rangle = 0.43$, respectively.

The conservation equations involve a reference state, which consists of a set of vertical profiles for the density, the thermal conductivity, and the temperature. These profiles are calculated using appropriate thermodynamic relationships[S15] and are plotted on Supplementary Fig. 3. Density and thermal expansion are scaled with respect to their surface values, and the temperature is scaled with respect to the super-adiabatic temperature difference across the system, $\Delta T_S$. The thermodynamic properties used to build the reference state are listed in Supplementary Table 1, together with other scalings and properties.

The viscosity depends on depth and temperature, but not on composition. Viscosity follows an Arrhenius function in temperature, and an exponential law in depth. An additional viscosity jump of 30 is imposed at 660 km depth. The viscosity is thus fully described as a function of depth $z$ and temperature $T$ by

$$\eta(z,T) = \eta_0 \left[1 + 29H(z-660)\right] \exp\left[\xi_z \frac{z}{D} + \xi_T \frac{\Delta T_S}{(T+T_{\mathrm{off}})}\right], \qquad (6)$$

where $\eta_0$ is a reference viscosity, $H$ is the Heaviside step function, $T_{off}$ the temperature offset (which is added to the temperature to reduce the viscosity jump across the top boundary), and $D$ the mantle thickness. The viscosity variations with depth and temperature are controlled by the logarithmic ratios $\xi_z$ and $\xi_T$, respectively. In all the calculations reported in this paper, the reference viscosity is defined at $z = 0$ and for the surface temperature of the adiabat (*i.e.* $T_{as} = 0.64\Delta T_S$), and we fixed $\xi_T = 13.816$, $\xi_z = 2.303$, and $T_{off} = 0.88\Delta T_S$, which leads to top to bottom thermal viscosity ratio of about 4000, and a bottom to top depth viscosity ratio of 300.

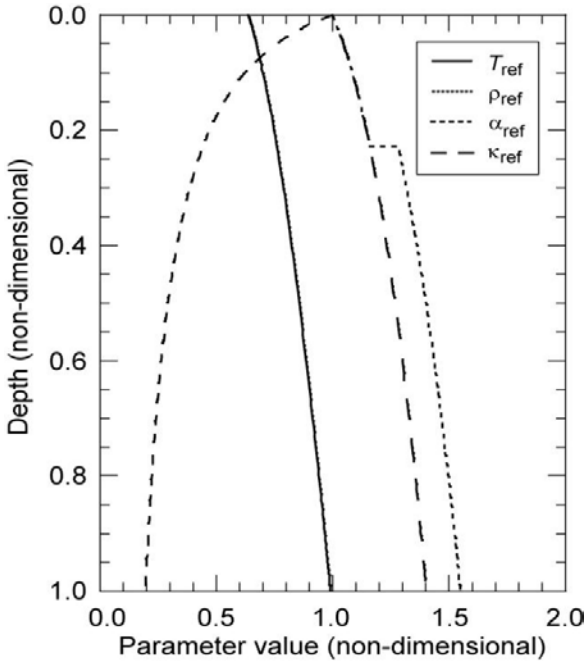


**Supplementary Figure 3 | Reference thermodynamic profiles.** $T_{ref}$, $\rho_{ref}$, $\alpha_{ref}$, and $\kappa_{ref}$ are the reference temperature, density, thermal expansion, and thermal diffusivity, respectively.

Because the fluid properties (viscosity, thermal expansion, thermal diffusivity and density) are allowed to vary throughout the system, the definition of the Rayleigh number is non-unique. At each time step, an effective Rayleigh number can be calculated from the average properties of the system. As input, however, one needs to prescribe a reference

DOI: 10.1038/NGEO1295

Rayleigh number calculated with reference values of the thermodynamic and rheological parameters. In our calculations, we prescribed a modified surface Rayleigh number defined with the surface values of the thermodynamic parameters and with the viscosity at the surface value of the adiabat ($T_{as} = 0.64\Delta T_S$),

$$Ra_S = \frac{\alpha_S \rho_S g \Delta T_S D^3}{\eta_0 \kappa_S}, \qquad (7)$$

where $\alpha_S$, $\rho_S$ and $\kappa_S$ the surface thermal expansion, density, and thermal diffusivity, respectively. The modified surface Rayleigh number remains constant during the entire run (the reference adiabat and the surface values of all parameters are assumed constant with time), and in all our calculations we fixed its value $Ra_S = 10^8$. This leads to values of effective Rayleigh number around $3.0\times10^6$ whatever the experiment, which is consistent with expected values of the Rayleigh number for the Earth's mantle (typically, $10^6 \leq Ra_{Mantle} \leq 10^7$).

The compositional field is modeled with a collection of 15 million particle tracers. We defined two types of particles, for the primitive and regular materials (representing the primitive reservoir and the pyrolitic mantle), respectively. The fraction of primitive material is controlled by prescribing the fraction of dense particles, which we fix to 10% in all experiments. Particles of primitive material are initially distributed in a layer at the bottom of the system. For geometrical reasons, the thickness of this layer is numerically equal to the fraction of primitive material (thus 0.1 in non-dimensional units, *i.e.* about 300 km when scaled to the Earth's mantle thickness). Tracers are advected following a 4$^{th}$ order Runge-Kutta method, and at each time step the compositional field is obtained by calculating the concentration $C$ of particles of primitive material in each cell. This concentration varies between 0 (for a cell filled with regular material only) and 1 (for a cell filled with primitive material only).

| Parameter | Symbol | Value | Units | Non-dimensional |
|---|---|---|---|---|
| *Non-dimensional parameters* | | | | |
| Reference Rayleigh number | $Ra_S$ | | | $10^8$ |
| Buoyancy ratio | $B_c$ | | | 0.14-0.26 |
| Volume fraction of dense material | $X$ | | | 0.1 |
| Surface dissipation number | $Di_S$ | | | 1.2 |
| Volume average dissipative number | $Di$ | | | 0.43 |
| Total internal heating | $H_C$ | 65 | mW $m^{-2}$ | 25 |
| Compositional heating ratio | $\Delta H_C$ | 10 | | |
| *Physical & thermo-dynamical parameters* | | | | |
| Acceleration of gravity | $g$ | 9.81 | m $s^{-2}$ | 1.0 |
| Mantle thickness | $D$ | 2891 | km | 1.0 |
| Initial thickness of primitive layer | $d_{prim}$ | 289.1 | km | 0.1 |
| Reference adiabat | $T_{as}$ | 1600 | K | 0.64 |
| Super-adiabatic temperature difference | $\Delta T_S$ | 2500 | K | 1.0 |
| Surface density | $\rho_S$ | 3300 | kg/$m^3$ | 1.0 |
| Surface thermal expansion | $\alpha_S$ | $5.0\times10^{-5}$ | $K^{-1}$ | 1.0 |
| Surface thermal diffusivity | $\kappa_S$ | $6.24\times10^{-7}$ | $m^2$ $s^{-1}$ | 1.0 |
| Heat capacity | $C_P$ | 1200 | J $kg^{-1}$ $K^{-1}$ | 1.0 |
| Surface conductivity | $k_S$ | 3.0 | W $m^{-1}$ $K^{-1}$ | 1.0 |
| Surface Grüneisen parameter | $\gamma_S$ | 1.091 | | |
| Density at 660 km | $\rho_{660}$ | 4300 | kg/$m^3$ | 1.3 |
| Thermal expansion at 660 km | $\alpha_{660}$ | $2.2\times10^{-5}$ | $K^{-1}$ | 0.44 |
| Density jump at $z$ = 660 km | $\Delta\rho_{660}$ | 400 | kg/$m^3$ | 0.1212 |
| Clapeyron slope at $z$ = 660 km | $\Gamma_{660}$ | -3.0 - 0.0 | MPa $K^{-1}$ | $-0.8\times10^{-1}$ - 0.0 |
| *Viscosity law* | | | | |
| Reference viscosity | $\eta_0$ | $1.6\times10^{21}$ | Pa s | 1.0 |
| Viscosity ratio at $z$ = 660 km | $\Delta\eta_{660}$ | 30 | | |
| Logarithmic thermal viscosity ratio | $\xi_T$ | 13.816 | | |
| Logarithmic vertical viscosity ratio | $\xi_z$ | 2.303 | | |
| Logarithmic compositional viscosity ratio | $\xi_C$ | 0 | | |
| *Dimensional scalings* | | | | |
| Velocity | $v$ | 1.0 | cm $yr^{-1}$ | 1468 |
| Time | $t$ | 424 | Gyr | 1.0 |
| Heat flux | $\Phi$ | 2.6 | mW $m^{-2}$ | 1.0 |
| Internal heating rate | $H$ | $2.72\times10^{-13}$ | W $kg^{-1}$ | 1.0 |

**Supplementary Table 1 | Parameters and scalings**

The main change compared to our previous experiments[S13,S14] concerns the definition of the chemical buoyancy ratio, $B_c$, which measures the chemical density contrast between the primitive and regular materials, and is here defined relatively to the surface density $\rho_S$,

DOI: 10.1038/NGEO1295

$$B_c = \frac{\Delta\rho_c}{\alpha_S \rho_S \Delta T_S} . \quad (8)$$

By contrast, in our previous studies the buoyancy ratio was defined relatively to the reference density profile $\rho(z)$, *i.e.* that for a fixed value of $B_c$ the chemical density contrast increases with depth. The definition of the buoyancy ratio has substantial influence on the dynamics of the system and on the thermo-chemical distributions. In particular, the value of $B_c$ required to obtain a chemical stratification of the system is larger when the surface density is taken as reference density. Furthermore, with this definition of $B_c$, small scale compositional anomalies are more easily generated and the topography of the dense reservoirs is less pronounced. However, general the conclusions concerning the role of physical and rheological parameters in the formation and survival of the dense reservoirs are similar to those made in our previous studies[S13,S14]. Values of $B_c$ for the Earth's mantle can be estimated from the chemical density anomalies inferred from probabilistic tomography[S4]. Peak to peak, these anomalies reach 1.5% with respect to PREM[S16], *i.e.* a density contrast of about 80.0 kg $m^{-3}$ (where we assumed an average density of the lowermost mantle $\rho_{LLM}$ = 5400 kg $m^{-3}$). Taking $\alpha_S = 5.0\times10^{-5}$ $K^{-1}$, $\rho_S$ = 3300 kg $m^{-3}$, and assuming $2000 \leq \Delta T_S \leq 3000$ K, $B_c$ for the Earth's mantle yields between 0.16 and 0.24. Note that this range does not account for uncertainties in observed density anomalies, and may be extended by 20-30%. In this study, we conducted experiments for values of $B_c$ in the range 0.14 – 0.26.

The phase change at 660 km is modeled with a discontinuous phase transition that is controlled by defining a point on the phase boundary and a Clapeyron slope, $\Gamma_{660}$. Here, we imposed $z$ = 660 km and $T$ = 1900 K as anchor point, and we varied $\Gamma_{660}$ between -3.0 and 0 MPa/K. The density contrast at the phase transition is $\Delta\rho_{660}$ = 400 kg/$m^3$ and is scaled with

the surface density. An endothermic phase transition induces some negative buoyancy, which is measured by the phase transition buoyancy ratio,

$$B_{\mathrm{PT}} = -\frac{\Gamma \Delta \rho_{\mathrm{PT}}}{\alpha_{\mathrm{PT}} \rho_{\mathrm{PT}}^2 g D} \ , \qquad (9)$$

where $\alpha_{PT}$, $\rho_{PT}$, and $\Delta\rho_{PT}$, are the thermal expansion, density, and density jump, at the phase transition. For the 660 km phase transition of the Earth's mantle, the thermodynamic reference model we used indicate that $\alpha_{660} = 2.2\times10^{-5}$ K$^{-1}$ and $\rho_{660} = 4300$ kg/m$^3$. Taking $\Delta\rho_{660} = 400$ kg/m$^3$, the phase transition buoyancy ratio at 660 km is $B_{PT} = -0.034\Gamma_{660}$ (with $\Gamma_{660}$ in MPa/K). The value of $\Gamma_{660}$ is still debated, a difficulty being that the mantle aggregate consists of several minerals whose transitions occur at different pressures and have different Clapeyron slopes. The 660 km transition is associated with the transformation of ringwoodite in perovskite and periclase, and the Calpeyron slope of this transition is between -3.0 and -2.0 MPa/K[S17-S20]. The transformation of garnets occurs at greater depths with a Clapeyron slope between +1.0 and +2.0 MPa/K[S19,S21]. Ringwoodite dominates the mantle aggregate between 520 and 660 km, and its transformation around 660 km constitutes a barrier for downwelling slabs and upwelling plumes around this depth, whatever the effect of garnets at greater depths. The most likely value for $\Gamma_{660}$, according to published experiments and calculations, should therefore be in the range $-3.0 \leq \Gamma_{660} \leq -2.0$ MPa/K. However, to account for the potential effects of garnet at greater depths, a larger range may be considered, typically $-3.0 \leq \Gamma_{660} \leq -1.0$ MPa/K. For these values, $B_{PT}$ yields between 0.102 and 0.034.

## Thermo-chemical distributions from numerical experiments

We conducted experiments of thermo-chemical convection for chemical buoyancy ratios between 0.14 and 0.26, and Clapeyron slopes of the 660 km phase transition between -3.0 and

DOI: 10.1038/NGEO1295

0.0 MPa/K. Each experiment is run up to a non-dimensional time of $2.12\times10^{-2}$, which corresponds to a dimensional time of 9.0 Gyr (see scaling in Table S1), and starts with a transient phase about 1.3 to 1.7 Gyr long, during which the basal dense layer is heating up and the whole system is stable. The actual Earth probably started very hot so this early phase would have been over very quickly, but the long term solution is not expected to be influenced by initial condition. As convection starts, large plumes are generated resulting in a pulse of entrainment of primitive material. The duration of this overshoot phase is typically of 0.8 Gyr. The system finally reaches a nearly equilibrium state, in which the flow pattern is slowly evolving. In particular plumes locations slightly oscillate around average positions. The long-term stable phase is reached at times of about 2.5 to 3.4 Gyr, depending on the case.

As in previous studies[S13,S14] we observe, after the transient and overshoot phases, the formation of thermo-chemical structures, whose shape and stability depend on the values of $B_c$ and $\Gamma_{660}$ (see main text and Fig. 2). It is important to derive quantitative features from the distributions in temperature and composition obtained by each model, to better describe them and test them against existing constraints (mainly from seismology). In particular, thermal and chemical contributions to the relative density anomalies can be calculated from the profiles of the horizontally averaged temperature and composition ($\bar{T}(z)$ and $\bar{C}(z)$),

$$dln\rho_T(x,y,z) = -\frac{\alpha[T(x,y,z)-\bar{T}(z)]}{[1-\alpha(\bar{T}(z)-T_S)+\alpha_S\Delta T_S B_c\bar{C}(z)]}\ , \qquad (10)$$

and $$dln\rho_c(x,y,z) = \frac{\alpha_S\Delta T_S B_c[C(x,y,z)-\bar{C}(z)]}{[1-\alpha(\bar{T}(z)-T_S)+\alpha_S\Delta T_S B_c\bar{C}(z)]}\ . \qquad (11)$$

First hints about the thermo-chemical structure can be deduced from the profiles of the RMS in $d\ln\rho_T$ and $d\ln\rho_c$. A strong chemical stratification results in a RMS of $d\ln\rho_c$ that peaks around the interface between the dense and regular materials and is zero elsewhere, whereas an efficient mixing leads to a RMS of $d\ln\rho_c$ that is small and does not vary with depth. Pools

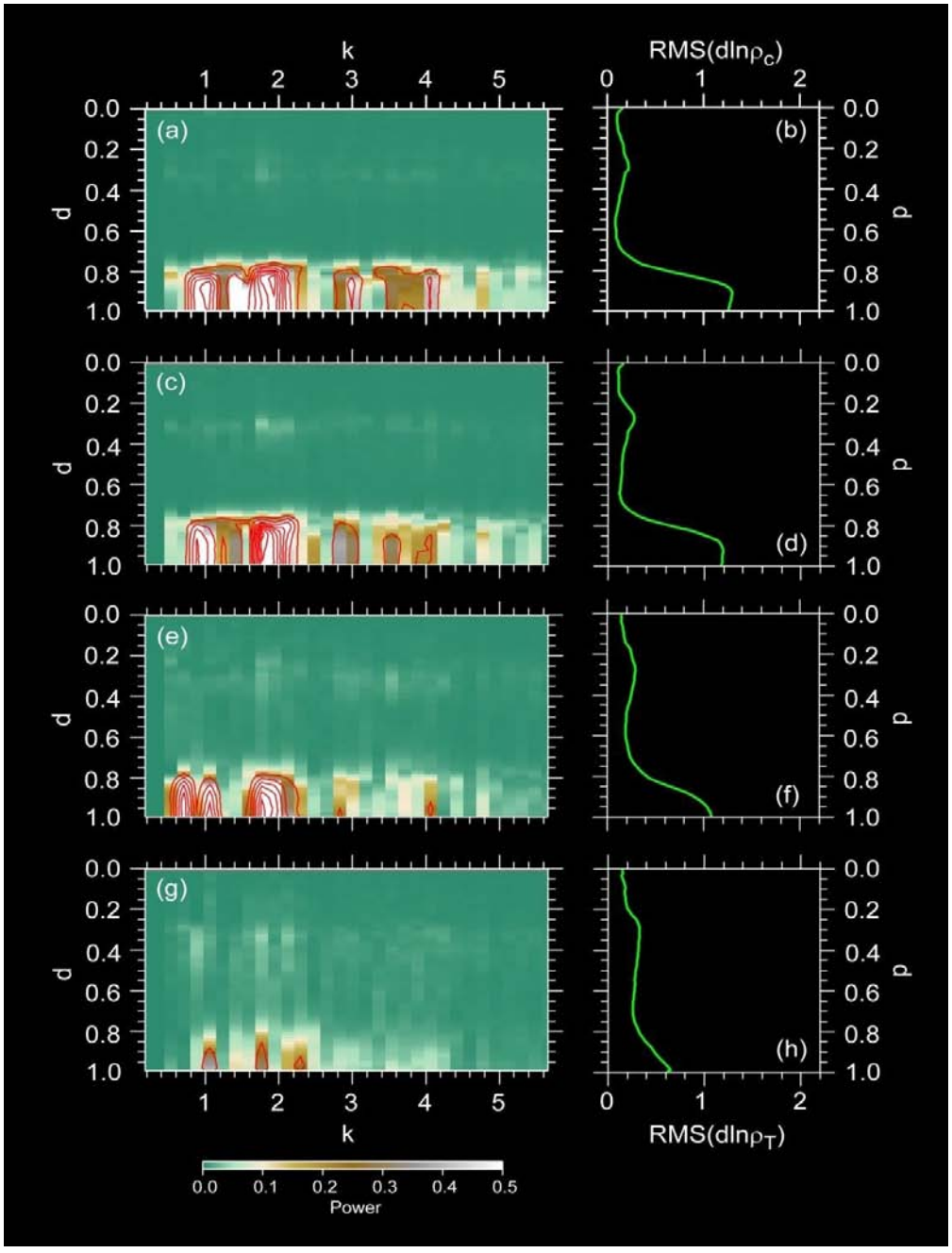


**Supplementary Figure 4 | Spectral heterogeneity maps (SHM, left column) and vertical profiles of RMS (right column) of chemical density anomalies for four cases.** (a-b) Buoyancy ratio $B_c = 0.22$, clapeyron slope of the phase transition at 660 km $\Gamma_{660} = -2.5$ MPa/K. (c-d) $B_c = 0.20$, $\Gamma_{660} = -2.5$ MPa/K. (e-f) $B_c = 0.20$, $\Gamma_{660} = -1.0$ MPa/K. (g-h) $B_c = 0.16$, $\Gamma_{660} = -2.5$ MPa/K. SHM are plotted with both a color scale and contour levels (red curves, interval is 0.2). *d* is the non-dimensional depth, scaled with $D = 2891$ km. All snapshots are taken at time $t = 6.3$ Gyr (non-dimensional time $t_{adim} = 1.48\times10^{-2}$).

DOI: 10.1038/NGEO1295

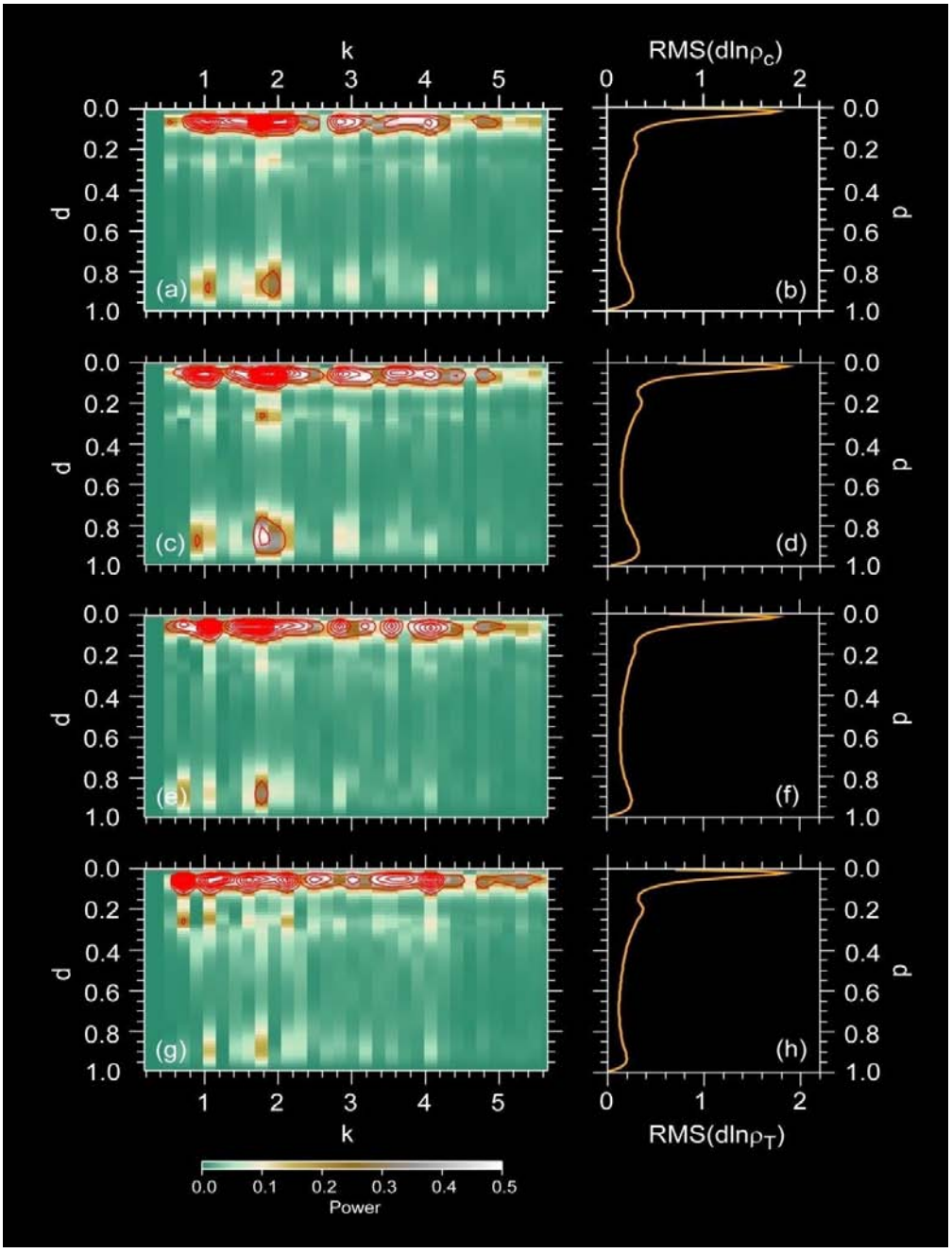


**Supplementary Figure 5 | Spectral heterogeneity maps (SHM, left column) and vertical profiles of RMS (right column) of thermal density anomalies for four cases.** (a-b) Buoyancy ratio $B_c$ = 0.22, and clapeyron slope of the phase transition at 660 km $\Gamma_{660}$ = -2.5 MPa/K. (c-d) $B_c$ = 0.20, $\Gamma_{660}$ = -2.5 MPa/K. (e-f) $B_c$ = 0.20, $\Gamma_{660}$ = -1.0 MPa/K. (g-h) $B_c$ = 0.16, $\Gamma_{660}$ = -2.5 MPa/K. SHM are plotted with both a color scale and contour levels (red curves, interval is 0.2). *d* is the non-dimensional depth, scaled with $D$ = 2891 km. All snapshots are taken at time $t$ = 6.3 Gyr (non-dimensional time $t_{adim}$ = $1.48\times10^{-2}$).

of dense material standing at the bottom of the system result in a RMS of $d\ln\rho_c$ that strongly varies with depth. The shape of the RMS profile depends however on the topography and lateral extension of the pools. Similarly, the arrival and spreading of plumes beneath the surface lead to a strong increase in the RMS of $d\ln\rho_T$. More detailed information can be inferred from spectral heterogeneity maps (SHM)[S22] of $d\ln\rho_T$ and $d\ln\rho_c$, which plot the 2D Fourier power spectra of these distributions as function of depth. Supplementary Figs. 4 and 5 show examples of RMS profiles and SHMs for four cases, including stable thermo-chemical pools and eroding thermo-chemical piles (note that in the SHMs plots, the 2D wave number $k$ is defined from the wave numbers along the $x$- and $y$- directions, $k = \sqrt{{k_x}^2 + {k_y}^2}$). Stable thermo-chemical pools induce strong chemical density anomalies at the bottom of the system. In contrast, eroding piles induce small to moderate chemical density anomalies (these anomalies are actually decreasing in amplitude with time, as shown below). Note that in all cases, strong thermal density anomalies due to the spreading of the plumes beneath the surface are present in the top part of the system.

It has been pointed out that the uncertainties and vertical parameterizations of tomographic models are such that RMS profiles alone may not be sufficient to discriminate between possible models of mantle convection[S23]. To decide whether a given model agrees with tomography, comparisons between power spectra of the observed and modeled density anomalies are needed. Because tomographic models are developed in spherical harmonics, relevant comparisons with observed density models requires to sum up the Fourier spectra of density anomalies over the wave number $k$. Noting that the power per surface unit must be equal in both Fourier and harmonic expansions, the signal contained in spherical harmonic degree $\ell$ is obtained by summing the 2D wave-number in the range[S24]

DOI: 10.1038/NGEO1295

$$\ell + \frac{1}{2} \leq kR \leq \ell + \frac{3}{2}, \qquad (12)$$

where $R$ is the Earth's radius. For comparison with probabilistic tomography, only spherical harmonic degrees 2, 4 and 6 are needed, and additional radial averaging according to the radial parameterization of probabilistic tomography must be performed. Fig. 2 compares the time evolution of the power spectra of thermal and chemical density anomalies in the lowermost layer ($2000 \leq z \leq 2891$ km) obtained for four cases, with the power spectra from probabilistic tomography (horizontal shaded areas). The power spectra of both the thermal and chemical density anomalies associated with the large pools fit well probabilistic tomography at any times (except, of course, during the initial transient phase). In contrast, the power spectra of the chemical density anomalies associated with eroding piles strongly decrease with time, and do not fit probabilistic tomography in the long term.

A measure of the erosion is given by the average altitude of dense material[S13],

$$\langle h_C \rangle = \frac{1}{\vartheta} \int (1 - z) C(x, y, z) d\vartheta, \qquad (13)$$

where $\vartheta$ is the total volume of the model. Initially, $<h_C>$ is equal to half the thickness of the initial layer, $d_{prim}/2$ (where $d_{prim} = 0.1D$ in all our calculations, and $D$ is the total thickness of the system, equal to 2891 km in the case of the Earth's mantle). By the end of the calculation the value of $<h_C>$ depends on the degree of mixing between the dense and regular material, and varies from $d_{prim}/2$ for cases with strong chemical stratification, to $D/2$ for cases with efficient mixing. In our experiments, $<h_C>$ is constant at $0.05D$ during the heating phase, peaks during the overshoot phase, and finally oscillates around a constant value when a nearly equilibrium state is reached (Fig. 3). At this stage, a value of $<h_C>$ around $0.5D$ indicates that regular and primitive materials are well mixed, *i.e.* pools have been severely or entirely eroded. By contrast, a value of $<h_C>$ significantly lower than $0.5D$, as observed for models

with $B_c$ = 0.22, indicates that pools experience only a slight erosion and remain stable over period of time comparable to the age of the Earth.

### Plume detection and mass fraction of primitive material in plumes

Small amounts of primitive material are entrained upwards in thermal plumes. An important quantity that can be related to geochemical observations and mass balance calculations is the entrainment of primitive material, *i.e.* the mass fraction of primitive material in plumes with respect to the total mass of the plume ($x_{PM}$). To estimate this fraction, we followed a two step approach. First, we applied a plume detection technique[S25] to the temperature distributions predicted by our models. A pixel is assumed to be part of the plume if its temperature satisfies

$$T(x,y,z) \geq \bar{T}(z) + c[T_{max}(z) - \bar{T}(z)] \,, \qquad (14)$$

where $T_{max}(z)$ is the maximum temperature at depth $z$, and $c$ a constant independent of depth. Choosing the value of $c$ is somehow arbitrary, and a too small (large) value will overestimate (underestimate) the size of the plume. We solved this problem by repeating calculations of $x_{PM}$ for several values of $c$ within a prescribed range. Assuming $0.4 \leq c \leq 0.6$, we found that the variance in $x_{PM}$ is around 0.3-0.6 %, depending on the case, which is smaller than the variance obtained by time-averaging (see below). Second, we calculate the ratio between the mass of primitive material in the detected plume and the total mass of these plumes following

$$x_{PM} = \frac{\sum_{x,y,z<660} \rho_{PM} C d\vartheta}{\sum_{x,y,z<660} \rho d\vartheta} = \frac{\sum_{x,y,z<660} C[1-\alpha_S \Delta T_S (T-T_S)+\alpha_S \Delta T_S B_c]}{\sum_{x,y,z<660}[1-\alpha_S \Delta T_S (T-T_S)+\alpha_S \Delta T_S B_c C]} \,, \qquad (15)$$

where d$V$, ρ, $\rho_{PM}$, $T$, and $C$ are the element volume, density, density of the primitive material, temperature and concentration in dense particles at a given location. Note that the summations in (Eq. 15) are restricted to the region located above the phase transition, representing the upper mantle in the case of the Earth. This ratio is varying with time, but once the nearly

DOI: 10.1038/NGEO1295

equilibrium flow has been reached, these changes remain small to moderate (Supplementary Fig. 6). To account for this possible source of uncertainty, we averaged $x_{PM}$ over the last third of the run, corresponding to a period of 3.0 Gyr. Resulting variances range from less than 1% up to about 6%, depending on the case. We use these variances as a measure of the error bar on $x_{PM}$.

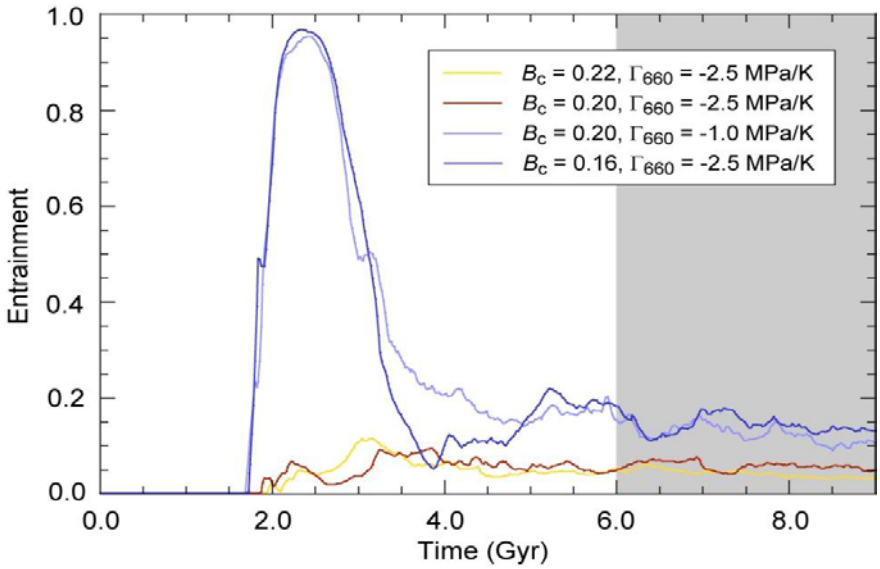


**Supplementary Figure 6 | Time evolution of the entrainment for four cases.** Entrainment is defined by Eq. 15. The cases considered are detailed in the legend, where $B_c$ is the buoyancy ratio and $\Gamma_{660}$ the clapeyron slope of the phase transition at 660 km). The grey shaded band indicates the time range in which entrainment was averaged out.

Both the chemical density contrast between primitive and regular materials and the endothermic phase change act as a negative buoyancy, *i.e.* oppose the upwards motion of primitive material and its penetration in the upper mantle. Our experiments indicate that $x_{PM}$ is mainly controlled by the chemical buoyancy ratio and to a lesser extent by the Clapeyron slope of the 660 km phase transition (Fig. 4). In experiments with $B_c \geq 0.22$ (corresponding to the stable pools), $x_{PM}$ is smaller than 7% whatever the value of $\Gamma_{660}$ we considered (except for $\Gamma_{660} = 0$), whereas in experiments with $B_c \leq 0.16$ (corresponding to the eroding piles), $x_{PM}$ is

larger than 11% for all the values of $\Gamma_{660}$ we considered. For intermediate values of $B_c$, the Clapeyron slope of the phase transition plays a significant role in controlling the entrainment of primitive material. If $\Gamma_{660}$ is low enough, the additional negative buoyancy provided by the endothermic phase transition prevents upwards flow of primitive material across the phase transition, and $x_{PM}$ keeps below 10%.

## Resolution tests

Quantifying the entrainment of primitive material accurately requires appropriate spatial resolution. The calculations we used to estimate the entrainment were performed on grids with 128×128×64 points and used 15 millions tracers, i.e. a concentration in tracers of about 15 tracers per cell. Resolution tests done in previous studies[S26] indicate that this grid size and concentration of tracers is sufficient. We performed additional tests (Supplementary Fig. 7) for the specific experimental setup designed in our calculations (see Geodynamic Modeling section), fixing $B_c$ = 0.22, $\xi_T$ = 13.816, and $\Gamma$ = -2.5 MPa/K. First, we tested different grid sizes and fixed the concentration in tracers to 15 tracers per cell (Supplementary Fig. 7a). For all grids, the aspect ratio is equal to 4, and the number of grid points in the x and y direction is twice that in the vertical direction. The measured entrainment strongly decreases with increasing resolution up to a grid with 96×96×48 points. For finer grids (up to 192×192×96 points), the entrainment slowly decreases but remains in the range 3.5-4.5 %. Second, we fixed the grid resolution to 128×128×64 points and varied the concentration of tracers (Supplementary Fig. 7b). The measured entrainment strongly increases up to a concentration of 10 tracers per cell. For larger values (up to 50 tracers per cell), the measured entrainment remains stable around 4%. Overall, the additional resolution tests we performed indicate that the grid resolution (128×128×64 points) and tracer concentration (15 tracers per cell) we used

DOI: 10.1038/NGEO1295

in our main series of experiments allow accurate measurements of the entrainment of dense material in plumes. Using better resolutions would induce discrepancies that are within the error bars estimated from the time variance of the entrainment.

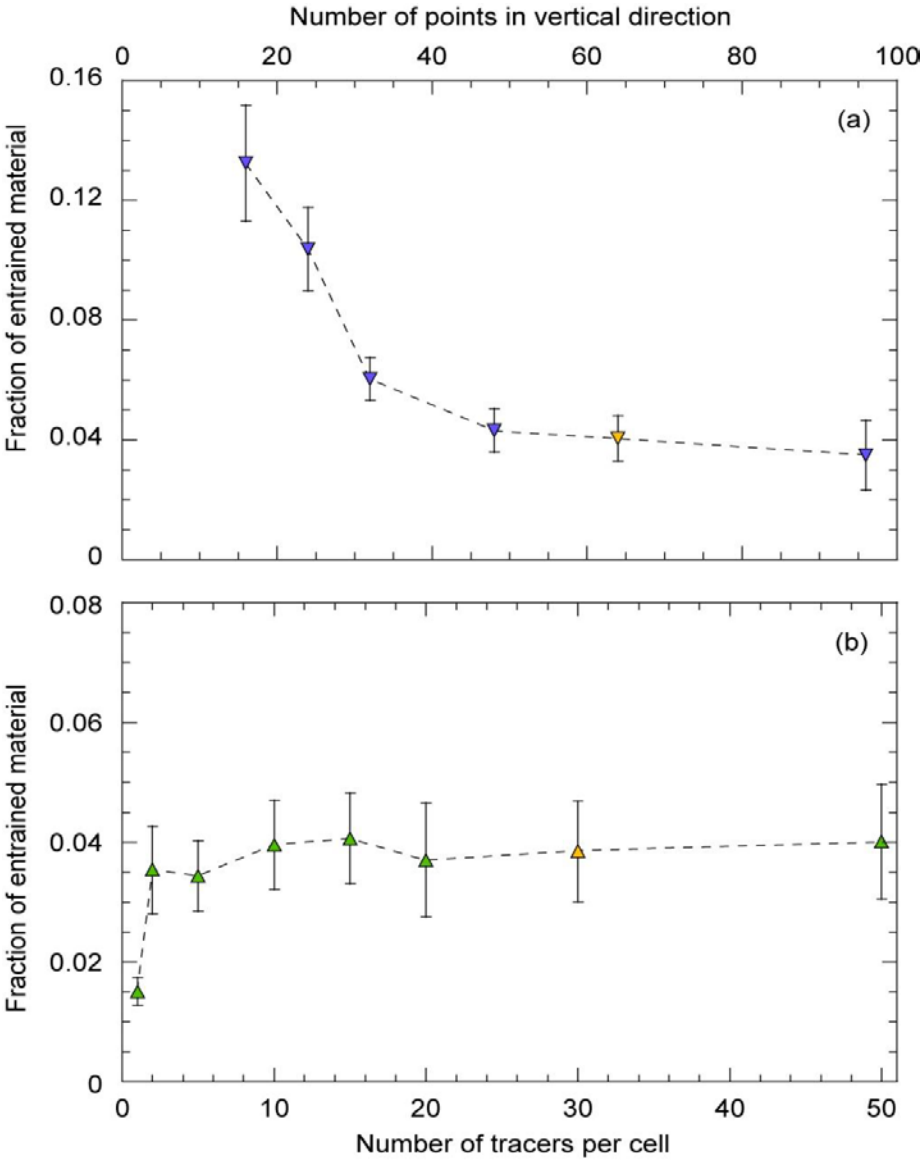


**Supplementary Figure 7 | Resolution tests.** (a) Entrainment as a function of the grid size. The average number of tracers per cell is 15 for all experiments. The *x*-axis represents the number of vertical points, *npz*. The number of points in the *x* and *y* direction is twice *npz*. (b) Entrainment as a function of the average number of tracers per cell. The grid size is 128×128×64 for all experiments. The resolution used in our main series of experiments is denoted by the orange symbol.

## Influence of thermal viscosity contrast and thermal expansion

Thermal viscosity contrast strongly influences the dynamics of primitive reservoir[S13]. If viscosity is kept constant with temperature, primitive reservoirs are swept out within a short (< 1 Gyr) period of time. The viscosity of mantle materials (including that of olivine and perovskite) is, however, strongly temperature dependent, this dependence being controlled by the activation energy of each mineral. It is therefore reasonable to include strong thermal viscosity variations in numerical models of mantle dynamics. To estimate the influence of the amplitude of thermal viscosity variations on the entrainment, we performed an additional series of calculations with values of the logarithmic thermal viscosity contrast $\xi_T$ (Eq. 6) between 0 and 23.026. This parameter models the activation energy $E_a = \xi_T \Delta T_S R$, where $\Delta T_S$ and $R$ = 8.32 are the super-adiabatic temperature jump and the ideal gas constant, respectively. In all additional experiments, the chemical buoyancy ratio and clapeyron slope at 660 km are fixed to $B_c$ = 0.22 and $\Gamma_{660}$ = -2.5 MPa/K, respectively. Supplementary Fig. 8 shows the entrainment as a function of $\xi_T$. For $\xi_T$ = 0 (viscosity does not depend on temperature) pools of dense material experience strong erosion, and the entrainment of primitive material reaches 16%. Erosion and entrainment then sharply decrease with increasing thermal viscosity contrast. For $\xi_T$ = 23.026 (activation energy around 480 kJ/mol) the entrainment has droped to 1%. The thermal viscosity contrast we imposed in our main calculations ($\xi_T$ = 13.816) is equivalent to an activation energy of about 290 kJ/mol, a conservative value for the lower mantle[S27]. For this value of $\xi_T$ entrainment is small, around 4%. According to our additional calculations, larger activation energies would lead to smaller entrainment, hence strengthening our main conclusion that OIB plumes partially sample a deep reservoir of primitive material.

DOI: 10.1038/NGEO1295

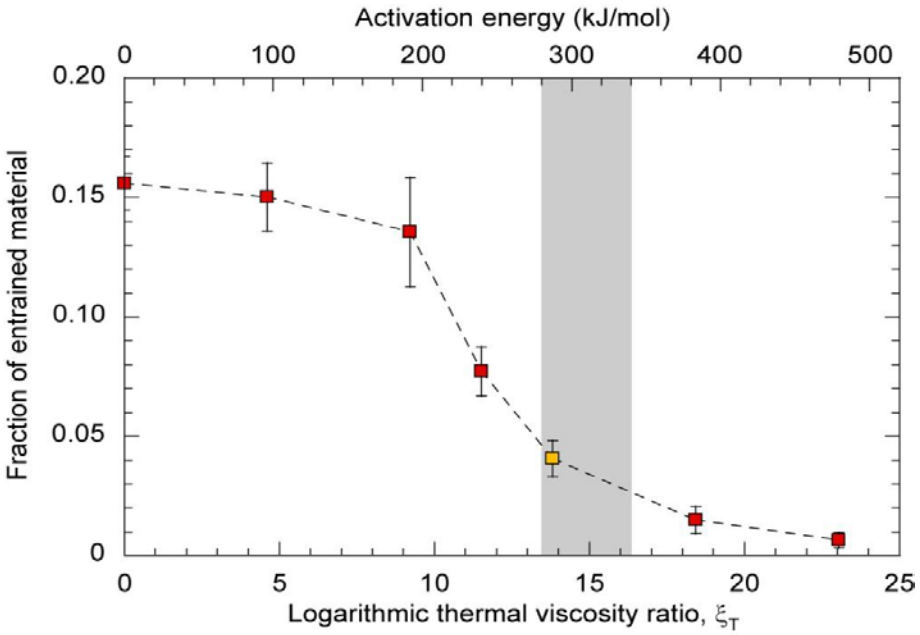


**Supplementary Figure 8 | Influence of the thermal viscosity contrast on the entrainment of dense material.** The buoyancy ratio and the clapeyron slope of the phase transition at 660 km are $B_c$ = 0.22 and $\Gamma_{660}$ = -2.5 MPa/K, respectively. Results are plotted both as a function of the logarithmic thermal viscosity contrast $\xi_T$ (bottom) and of the corresponding activation energy (top). The shaded band covers a possible range of activation energy for lower mantle aggregate[S27]. The thermal viscosity contrast used in our main series of experiments is denoted by the orange symbol.

Thermal expansion $\alpha$ controls thermal buoyancy, and its variations with pressure and temperature may influence the dynamics of the primitive reservoirs. Our models account for the variations of $\alpha$ with depth through the prescription of a reference profile in the momentum and energy conservative equations[S15]. The reference $\alpha$ decreases by a factor 5 from top to bottom (Supplementary Fig. 3), i.e. thermal buoyancy strongly decreases with depth. This promotes chemical buoyancy, allowing the survival of reservoirs of dense material or, if the buoyancy ratio is strong enough, a chemical stratification. As discussed in the modelling section, we used a definition of the buoyancy ratio based on the surface values of thermodynamic paramaters (Eq. 9). If defined relative to the radial reference thermal expansion, the buoyancy ratio decrease with increasing depth. This decrease is however

partially balanced by the increase in reference density (Supplementary Fig. 3). Compared to a definition based on the vertical profile these parameters, our approach may thus induce small differences in the topology of the primitive reservoirs, but may not modify the stability of these reservoirs. Thermal expansion also varies with temperature, but our models do not account for these variations. At ambient pressure, thermal expansion of $MgSiO_3$ perovskite increase with temperature and is well fitted by

$$\alpha_s(T) = a_1 + a_2 T + \frac{a_3}{T^2} \quad , \qquad (16)$$

with $a_1$ = 2.066×10$^{-5}$ K$^{-1}$, $a_2$ = 0.909×10$^{-8}$ K$^{-1}$, and $a_3$ = -0.418 K[S28]. Assuming that a similar increase holds at high pressure, a 2500 K super-adiabatic temperature jump would result in a doubling of $\alpha$ from top to bottom, hence partially balancing the effect of pressure. Lateral variations in temperature of 500 K would induce a 10% change in $\alpha$. Because in our models primitive reservoirs appear hotter than average (Fig. 1), their $\alpha$ would be slightly larger than in the surrounding mantle. Overall, the effect of temperature on thermal expansion opposes the chemical buoyancy, and a slightly larger (say, 10-20%) buoyancy ratio may be required to keep primitive reservoirs stable. Such increase is accommodated by uncertainties in observed density anomalies[S4] (see modelling section). Additional modelling is of course needed to accurately quantify the influence of a temperature-dependent thermal expansion, but one may note that an increase in $B_c$ *a priori* reduces the entrainment. Finally, it is worth noting that thermal expansion may also depend on chemistry. Using $a_1$ = 3.681×10$^{-5}$ K$^{-1}$, $a_2$ = 0.9283×10$^{-8}$ K$^{-1}$, and $a_3$ = -0.7445 K[S29], the thermal expansion of periclase (MgO) at ambient pressure and temperature is larger than that of perovskite by about 70%. Therefore, assuming that primitive reservoirs are enriched in perovskite, as suggested by probabilistic tomography[S4], and if the difference between the thermal expansion of perovskite and periclase still holds at

DOI: 10.1038/NGEO1295

lower mantle pressure, the thermal variations of the thermal expansion would be partially balanced by its variations with composition.

## References

S1. Connolly, J.A.D. Computation of phase equilibria by linear programming: A tool for geodynamic modeling and its application to subduction zone decarbonation. *Earth Planet. Sci. Lett.* 236, 524-541 (2005).

S2. Stixrude, L. & Lithgow-Bertelloni, C. Thermodynamics of mantle minerals – II. Phase equilibria. *Geophys. J. Int.* 184, 1180-1213 (2011).

S3. Nakagawa, T., Tackley, P.J., Deschamps, F. & Connolly, J.A.D. The influence of MORB and harzburgite composition on thermo-chemical mantle convection in 3-D spherical shell with self-consistently calculated mineral physics. *Earth Planet. Sci. Lett.* 296, 403-412 (2010).

S4. Trampert, J., Deschamps, F., Resovsky, J.S. & Yuen, D.A. Probabilistic tomography maps significant chemical heterogeneities in the lower mantle. *Science* 306, 853-856 (2004).

S5. Javoy, M., Kaminski, E., Guyot, F., Andrault, D., Sanloup, C., Moreira, M., Labrosse, S., Jambon, A., Agrinier, P., Davaille, A. & Jaupart, C. The chemical composition of the Earth: Enstatite chondrite model. *Earth Planet. Sci. Lett.* 293, 259-268, (2010).

S6. Nomura, R., Ozawa, H., Tateno, S., Hirose, K., Hernlund, J., Muto, S., Ishii, H. & Hiraoka, N. Spin crossover and iron-rich silicate melt in the Earth's deep mantle. *Nature* 473, 199-203 (2011).

S7. Allègre, C.J. & Moreira, M. Rare gas systematic and the origin of oceanic islands: the key role of entrainment at the 670 km boundary layer. *Earth Planet. Sci. Lett.* **228**, 85-92 (2004).

S8. Kurz, M.D., Jenkins, W.J., Schilling, J.-G. & Hart, S.R. Helium isotopic variation in the mantle beneath the central North Atlantic Ocean. *Earth Planet. Sci. Lett.* **58**, 1-14 (1982).

S9. Sarda, P., Moreira, M., Staudacher, T., Schilling, J.-G. & Allègre, C.-J. Rare gas systematics on the southernmost Mid-Atlantic Ridge: constraints on the lower mantle and the Dupal source. *J. Geophys. Res.* **105**, 5973-5996 (2000).

S10. Moreira, M. & Allègre, C.-J. Rare gas systematic on Mid-Atlantic Ridge (37° – 40°). *Earth Planet. Sci. Lett.* **198**, 401-416 (2002).

S11. Stuart, F.M, Lass-Evans, S., Fitton, J.G. & Ellam, R.M. High $^{3}He/^{4}He$ ratios in picritic basalts from Baffin Island and the role of a mixed reservoir in mantle plumes. *Nature* **424**, 57-59 (2003).

S12. Tackley, P.J. Modelling compressible mantle convection with large viscosity contrasts in a three-dimensional spherical shell using the yin-yang grid. *Phys. Earth Planet. Inter.* **171**, 7-18 (2008).

S13. Deschamps, F. & Tackley, P.J. Exploring the model space of thermo-chemical convection I – Principles and influence of the rheological parameters. *Phys. Earth Planet. Inter.* **171**, 357-373 (2008).

S14. Deschamps, F. & Tackley, P.J. Exploring the model space of thermo-chemical convection II – Influence of physical and compositional parameters. *Phys. Earth Planet. Inter.* **176**, 1-18 (2009).

DOI: 10.1038/NGEO1295

S15. Tackley, P.J. Three-dimensional simulations of mantle convection with a thermo-chemical CMB boundary layer: D"? In: M. Gurnis et al. (Eds.), The Core-Mantle Boundary Region. *Geodynamical Ser.* **28**, 231-253 (1998).

S16. Dziewonski, A.M. & Anderson, D.L. Preliminary Reference Earth Model. *Phys. Earth Planet. Inter.* **25**, 297-356 (1981).

S17. Bina, C.R. & Helffrich, G. Phase transitions Clapeyron slopes and transition zone seismic discontinuity tomography. *J. Geophys. Res.* **99**, 15853-15860 (1994).

S18. Chopelas, A., Boehler, R. & Ko, T. Thermodynamics of γ-$Mg_2SiO_4$ from Raman spectroscopy at high pressure: the $Mg_2SiO_4$ phase diagram. *Phys. Chem. Minerals* **21**, 351-359 (1994).

S19. Hirose, K. Phase transitions in pyrolitic mantle around 670-km depth: implications for upwelling of plumes from the lower mantle. *J. Geophys. Res.* **107**, B02078 (2002).

S20. Yu, Y.G., Wentzcovitch, R.M., Tsuchiya, T., Umemoto, K. & Weidner, D. J. First principles investigation of the postspinel transition in $Mg_2SiO_4$. *Geophys. Res. Lett.* **34**, L10306 (2007).

S21. Akaogi, M. & Ito, E. Calorimetric study on majorite-perovskite transition in the system $Mg_4Si_4O_{12}$–$Mg_3Al_2Si_3O_{12}$: transition boundaries with positive pressure–temperature slopes. *Phys. Earth Planet. Inter.* **114**, 129-140 (1999).

S22. Tackley, P.J., Stevenson, D.J., Glatzmaier, G.A. & Schubert, G. Effects of multiple phase transitions in a three dimensional spherical model of convection in the Earth's mantle. *J. Geophys. Res.* **99**, 15877-15901 (1994).

S23. Deschamps, F., Trampert, J. & Tackley, P.J. Thermo-chemical structure of the lower mantle: seismological evidences and consequences for geodynamics, in D.A. Yuen et al. Eds., *Superplumes: beyond plate tectonics*, Springer, pp. 293-320 (2007).

S24. Chevrot, S., Montagner, J.-P. & Snieder, R. The spectrum of tomographic Earth models. *Geophys. J. Int.* **133**, 783–788 (1998).

S25. Labrosse, S. Hotspots, mantle plumes and core heat loss. *Earth Planet. Sci. Lett.* **199**, 147-156 (2002).

S26. Tackley, P.J. & King, S.D. Testing the tracer ratio method for modelling active compositional fields in mantle convection simulations. *Geochem. Geophys. Geosys.* 4, Q08302 (2003).

S27. Yamazaki, D., & Karato, S.I. Some mineral physics constraints on the rheology and geothermal structure of Earth's lower mantle. *Am. Mineral.* 86, 385-391 (2001).

S28. Oganov, A.R., Brodholt, J.P. & Price, G.D. Ab ignition elasticity and thermal equation of state of $MgSiO_3$ perovskite. *Earth Planet. Sci. Lett.* 184, 555-560 (2001).

S29. Suzuki, I. Thermal expansion of periclase and olivine and their anharmonic properties. *J. Phys Earth* 23, 145-159 (1975).